

Article

On a Response Surface Analysis: Hydrodeoxygenation of Phenol over a CoMoS-Based Active Phase

Itzayana Pinzón-Ramos ^{1,2}, Carlos O. Castillo-Araiza ^{2,*} , Jesús Andrés Tavizón-Pozos ³ 
and José Antonio de los Reyes ^{1,*}

¹ Laboratory of Environmental Catalysis, Universidad Autónoma Metropolitana-Iztapalapa, Av. San Rafael Atlixco 186, Col. Vicentina, Ciudad de Mexico 09340, Mexico

² Laboratory of Catalytic Reactor Engineering Applied to Chemical and Biological Systems, Universidad Autónoma Metropolitana-Iztapalapa, Av. San Rafael Atlixco 186, Col. Vicentina, Ciudad de Mexico 09340, Mexico

³ Investigadoras e Investigadores por México del CONACyT, Área Académica de Química, Universidad Autónoma del Estado de Hidalgo, Carr. Pachuca-Tulancingo Km. 4.5, C.P., Pachuca 42184, Mexico

* Correspondence: coca@xanum.uam.mx (C.O.C.-A.); jarh@xanum.uam.mx (J.A.d.l.R.)

Abstract: This work aims at assessing the hydrodeoxygenation (HDO) of phenol over a promising catalytic material: a CoMoS-based active phase with a Co/(Co + Mo) = 0.2, supported on a promising mixed oxide, Al₂O₃-TiO₂ (Al/Ti = 2). Particularly, to optimize the catalytic and kinetic performance of CoMoS/Al₂O₃-TiO₂, a response surface methodology (RSM) is carried out by following a Box–Behnken experimental design. The response variables are the initial reaction rate and the reaction selectivity, determined via a proper contribution analysis (φ) of both the direct hydrodeoxygenation (DDO) and the hydrogenation (HYD). At the same time, the operating conditions used as factors are the reaction temperature (280–360 °C), the total pressure (3–5.5 MPa), and the Mo loading (10–15 wt.%). The activity and selectivity are correlated to the catalysts' physicochemical properties determined by XRD, UV-Vis DRS, TPR, and Raman Spectroscopy. Regarding the CoMo-based active phase, a Mo loading of 12.5 wt.% leads to the optimal reaction performance, which is associated with the lowest (Co + Mo)^{oh}/(Co + Mo)th ratio. Concerning the operating conditions, a temperature of 360 °C and a total pressure of 5.5 MPa give rise to the optimal initial reaction rates, in which the DDO (φ = 65%) is selectively favored over HYD (φ = 35%).

Keywords: hydrodeoxygenation; CoMo-based active phase; phenol; optimization; RSM



Citation: Pinzón-Ramos, I.; Castillo-Araiza, C.O.; Tavizón-Pozos, J.A.; de los Reyes, J.A. On a Response Surface Analysis:

Hydrodeoxygenation of Phenol over a CoMoS-Based Active Phase.

Catalysts **2022**, *12*, 1139. <https://doi.org/10.3390/catal12101139>

Academic Editors: Hugo de Lasa and Mohammad Mozahar Hossain

Received: 7 September 2022

Accepted: 23 September 2022

Published: 28 September 2022

Publisher's Note: MDPI stays neutral with regard to jurisdictional claims in published maps and institutional affiliations.



Copyright: © 2022 by the authors. Licensee MDPI, Basel, Switzerland. This article is an open access article distributed under the terms and conditions of the Creative Commons Attribution (CC BY) license (<https://creativecommons.org/licenses/by/4.0/>).

1. Introduction

The generation of greenhouse gases through the burning of fossil-based fuels, and their contribution to global warming and climate change, has given rise to the exploration of alternate fuel-production processes [1]. In this regard, second-generation biofuels (hereafter called bio-oils), obtained from the pyrolysis of lignocellulosic biomass, including agro-industrial, agricultural or wood residues, have, nowadays, become attractive for substituting fossil-based fuels [2,3]. Although these bio-oils contain a low amount of nitrogen (0–0.2 wt.%) and sulfur-heteroatoms (<0.1 wt.%) their oxygen content is significantly high (35–40 wt.%) in comparison with fossil-based fuels. This oxygen content leads to undesired properties such as high viscosity, corrosivity, chemical and thermal instability, and the risk of polymerization [4–6]. Therefore, these properties restrict the use of bio-oils as transportation fuels, making their upgrading mandatory by eliminating oxygen-heteroatoms through proper catalytic treatments.

Catalytic hydrodeoxygenation (HDO) has been identified as one of the most promising approaches to upgrading bio-oils due to its ability to remove oxygen-heteroatoms from several bio-oil-based molecules [7,8]. The attractiveness of HDO rests on its similarity to the

well-known commercial catalytic hydrodesulfurization (HDS) of fossil-based fuels. For instance, as in the HDS process, the commercial CoMoS or NiMoS-based material, supported on γ -Al₂O₃, has been identified as active during the HDO of different oxygenated-based molecules [9–11]. Moreover, the operation conditions involved during the HDO, i.e., temperature and pressure, are similar to those applied during HDS. Specifically, HDO has been evaluated in broader temperature and pressure ranges: 200 to 400 °C and 0.1 to 20 MPa, respectively. Nevertheless, after two and half decades of assessing the HDO of different oxygenated molecules and catalytic systems, the main challenge relies on designing a highly active material and identifying the operating conditions for optimal kinetic performance [12–15].

It is accepted that the active sites of CoMoS and NiMoS-based catalysts are composed of the Mo-edge and coordinately unsaturated sites (CUS). Mo-edge active sites are selective for hydrogenation (HYD), whereas the promoted edges of the MoS₂ slabs are selective for the direct hydrodeoxygenation (DDO) [16–22]. The active phase suffers inhibition and deactivation because of the strong interaction between the support and oxygenated-based molecules [17]. In this regard, due to the lack of sulfur in the bio-oil composition, the catalysts tend to deactivate. Research works related to the deactivation mechanisms of either CoMoS or NiMoS-based active phase supported on γ -Al₂O₃ can be found in several contributions from the literature [9,10,16,17,19,23], including the ones from our research group [24–26].

To the above end, different strategies have been implemented to overcome inhibition and deactivation and, hence, increase activity during HDO [12,14,22,27–38]. In one of the most attractive proposals, different types of support have been proposed for the HDO to minimize catalyst deactivation [39–44], such as Al₂O₃, TiO₂, SiO₂, MgO, ZrO₂, CeO₂, Al₂O₃-TiO₂, ZrO₂-TiO₂, SiO₂-TiO₂, among others [15,17,32,45,46]. The selection of the appropriate support has improved the stabilization and activity of either the CoMoS or NiMoS active phase due to an improvement in the electronic metal-support interaction and the textural properties [17]. The use of Al₂O₃ has led to the strong adsorption of oxygenated-based molecules by its strong Lewis acid sites, causing coke formation on the surface and, subsequently, catalyst deactivation [19,22,47], while mixed-oxide-based supports have led to better results than pure oxides [24,25,48–53]. The Al₂O₃-TiO₂ support [51,54,55] has improved the catalytic performance of either the CoMoS or NiMoS-based active phase by increasing the activity and minimizing deactivation. On this basis, contributions from our research group [48] identified that a CoMo/Al₂O₃-TiO₂ catalytic system with an Al/Ti of 2 and a Mo loading of 15 wt.% during the HDO of phenol presented higher activities, and more resistance to sulfur, than CoMo/Al₂O₃-based mixed oxides. Although the research elucidated how the activity is improved and deactivation minimized, it was impossible to identify the Mo loading and operating conditions leading to optimizing the kinetic performance of CoMo/Al₂O₃-TiO₂ during the HDO of phenol.

This work is aimed to optimizing the catalytic performance of a promising CoMoS-based active phase supported on Al₂O₃-TiO₂ (Al/Ti = 2 or hereafter named AT2) with a Co/(Co + Mo) = 0.2 during the HDO of phenol, a stable oxygenated-based molecule within the composition of bio-oils. It is worth mentioning that the evaluation of phenol allows the obtention of relevant, quick, and straightforward information about the catalytic and kinetic functionalities of the catalysts regarding the cleavage of the C_{AR}-O bond on the catalytic surface [56]; such that results based on the use of phenol can be applied as the base for carrying out the HDO of different oxygenated-based molecules [52,57,58]. To achieve this aim, a response surface methodology (RSM) based on the Box–Behnken experimental design is implemented to identify the Mo loading in the CoMoS active phase and the operating conditions leading to the optimal performance of CoMo/AT2. The variables used as responses are the initial reaction rate and selectivity, while the factors, operating conditions, are the reaction temperature (280–360 °C), the total pressure (3–5.5 MPa), and the Mo loading (10–15 wt.%). The catalyst activity and selectivity are associated with some of the physical properties of AT2, determined by N₂ physisorption and XRD, and the chemical

characteristics of the CoMo-based active phase supported on AT2, determined by DRS UV-Vis, TPR, and Raman Spectroscopy. Results accounting for the catalyst characterization and surface response analysis are, firstly, presented in Section 2; secondly, their discussion is stated in Section 3; then, the methodology is given in Section 4; and, finally, Section 5 mentions the main conclusions and perspectives.

2. Results

2.1. Catalyst Characterization

Figure 1 displays the N₂ adsorption–desorption isotherm and X-ray diffractogram for the AT2 support. Based on the IUPAC classification [59], AT2 relates to a type IV isotherm with an H2b hysteresis, which means that AT2 presents a pore network with an area equal to 347 m²/g. The Barret–Joyner–Hallender (BJH) method shows that the average pore diameter and volume are 7.0 nm and 0.49 cm³/g, respectively. Moreover, the absence of well-defined peaks in the diffractogram elucidates the predominantly microcrystalline structure of AT2, confirming that the support is a mixed oxide. The pattern identified between 20° and 38° is associated with the presence of TiO₂ as microcrystals dispersed in the alumina matrix [24,51].

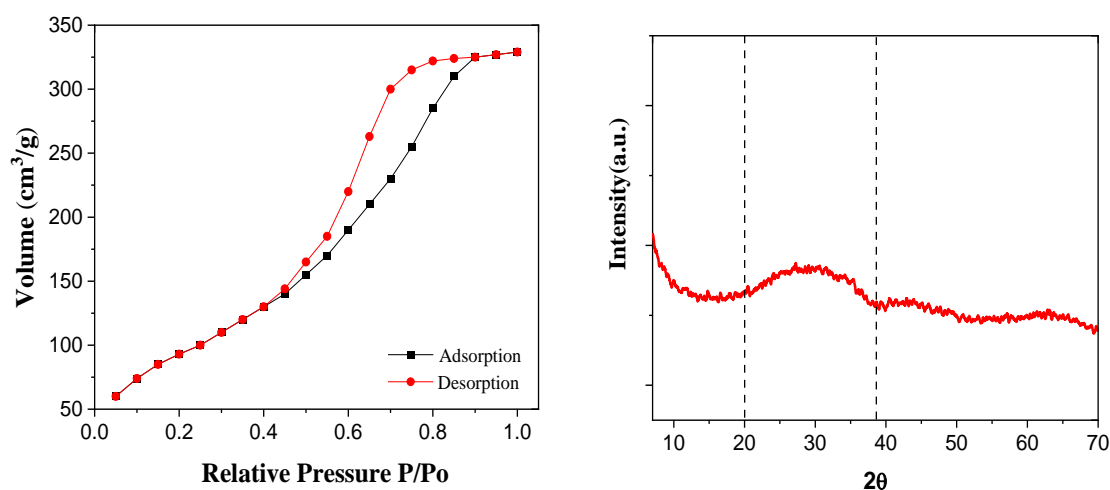


Figure 1. N₂ adsorption–desorption isotherm (left) and X-ray diffractogram (right) for the support Al₂O₃-TiO₂ (AT2).

Figure 2 displays the UV-Vis (DRS UV-Vis) spectra from 200 nm to 450 nm for the calcined Mo/AT2 and CoMo/AT2 catalysts when varying the Mo loading: 10, 12 and 15 wt.%. Absorption bands between 220 and 280 nm are attributed to Mo species in tetrahedral coordination (Moth) [39,43], while absorption bands from 290 to 350 nm are related to MoO_x species in their octahedral coordination (Mo^{oh}) [60,61]. Absorption bands from 200 to 360 nm are also associated with ligand-to-metal charge transfer (LMCT) for O²⁻ → Mo⁶⁺ [62,63]. Nonetheless, it is important to mention that the bands between 250 and 330 nm are related to LMCT for O²⁻ → Ti⁴⁺ [62], which overlap with those bands associated with Moth and Mo^{oh} species [61]. It is worth noting that while the Mo content increased, the spectrum signals shifted to visible light, indicating how Mo^{oh} species are formed with the increase of metal loading.

Moreover, by analyzing the absorption spectra from 200 to 800 nm for the CoMo/AT2 catalysts, it is possible to identify for all Mo loadings a shoulder from 480 to 800 nm due to the presence of Co. The absorption bands from 480 to 750 nm are associated with the electronic transitions for Co (II) with tetrahedral (Coth, 480–600 nm) and octahedral coordination (Co^{oh}, 600–750 nm). Moreover, the absorption bands from 400 to 500 nm, are associated with Co^{oh} species, Co (III), which are barely overlapped with Mo^{oh} species identified from 290 to 350 nm [60–63]. Nonetheless, the displacement of the bands towards

visible light is due to the increase in Mo and Co content due to the increment of Co^{oh} species in the active phase of the material.

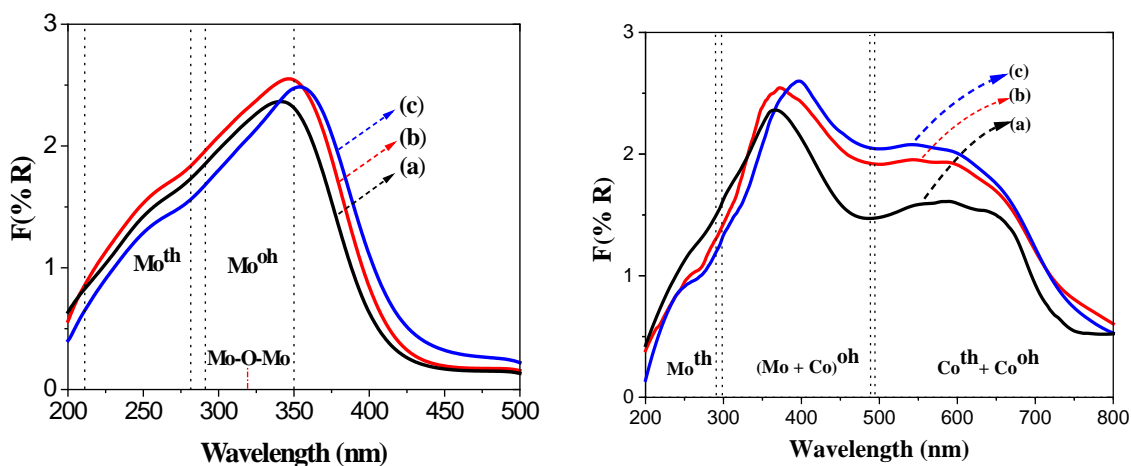


Figure 2. Diffuse reflectance UV-vis spectra of the Mo/AT2 (left) and CoMo/AT2 (right) catalysts accounting for different loadings of Mo: (a) 10, (b) 12 and (c) 15 wt.%.

TPR results of the Mo/AT2 and CoMo/AT2 catalysts with different Mo loadings are shown in Figure 3. In all samples, it is possible to identify three prominent reduction peaks. The reduction peak of Mo/AT2 catalysts near 400 °C indicates the reduction of $\text{Mo}^{6+} \rightarrow \text{Mo}^{4+}$ in octahedral coordination. The second peak, around 650 °C, is attributed to the reduction processes $\text{Mo}^{6+} \rightarrow \text{Mo}^{4+}$ and $\text{Mo}^{4+} \rightarrow \text{Mo}^0$ from the mixture of Mo species in octahedral and tetrahedral coordination [53]. Finally, at high temperatures (>600 °C), the reduction of $\text{Mo}^{4+} \rightarrow \text{Mo}^0$ in tetrahedral coordination and the TiO_2 (850 °C) from the support takes place [11,22,53]. The deconvolution analysis shows that octahedral Mo species increase their concentration in loadings higher than 10 wt.%. Additionally, the shift to lower temperatures of the middle peak indicates that Mo^{oh} species are easily reducible, i.e., Mo-based materials with a loading of 12 and 15 wt.% will be sulfided easier than with 10 wt.%, due to a decrease in the metal support interaction.

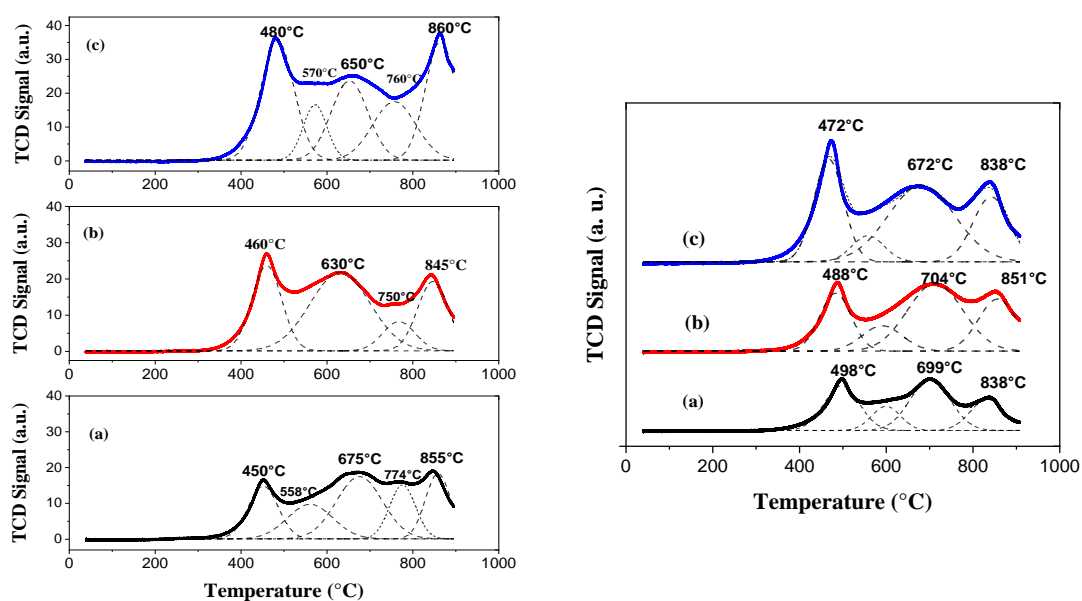


Figure 3. TPR profiles for the Mo/AT2 catalysts (left) and the CoMo/AT2 catalyst (right) with different Mo loadings: (a) 10, (b) 12, and (c) 15 wt.%.

Concerning the CoMo/AT2 catalyst, the peak between 470 and 498 °C is related to $\text{Co}^{3+} \rightarrow \text{Co}^{2+}$ and $\text{Mo}^{6+} \rightarrow \text{Mo}^{4+}$ reduction processes of Co^{oh} and Mo^{oh} species [53,64,65]. The peaks between 672 and 800 °C are associated with the total reduction of Co and Mo in tetrahedral coordination and CoMoO_4 species [11,48,66]. The peak at temperatures higher than 800 °C is related to the reduction of $\text{Ti}^{4+} \rightarrow \text{Ti}^{3+}$ [54]. Note that when the Mo content increases, the reduction peaks shift to lower temperatures indicating a decrease in the metal-support interaction. Moreover, the area of the first reduction peak increases with the Mo and Co content, indicating how a high Mo loading leads to a high formation of Co^{oh} and Mo^{oh} species in the active phase.

Raman spectra obtained for the Mo/AT2 and CoMo/AT2 catalysts are displayed in Figure 4. Regarding the Mo/AT2 material, four peaks are located at 992, 950, 817, and 665 cm^{-1} . The peak at 992 cm^{-1} (1) is attributed to the vibrations of octamolybdate species ($\text{Mo}_8\text{O}_{26}^{4-}$) [67]. The signal at 955 cm^{-1} (2) is assigned to vibrations of the Mo=O terminal bond associated with heptamolybdate species ($\text{Mo}_7\text{O}_{24}^{6-}$) [67–69]. The intensity of this peak increases according to the Mo content. The peak at 817 cm^{-1} (3) is assigned to the species of vibrations of monomeric molybdenum trioxide (MoO_3) [67,70]. The peak at 665 cm^{-1} (4) is also attributed to heptamolybdate species ($\text{Mo}_7\text{O}_{24}^{6-}$), but gives information on the stretching and bending vibrations of the internal M-O-M bond. Note that the intensity of peak 4 is not affected by the Mo loading [53].

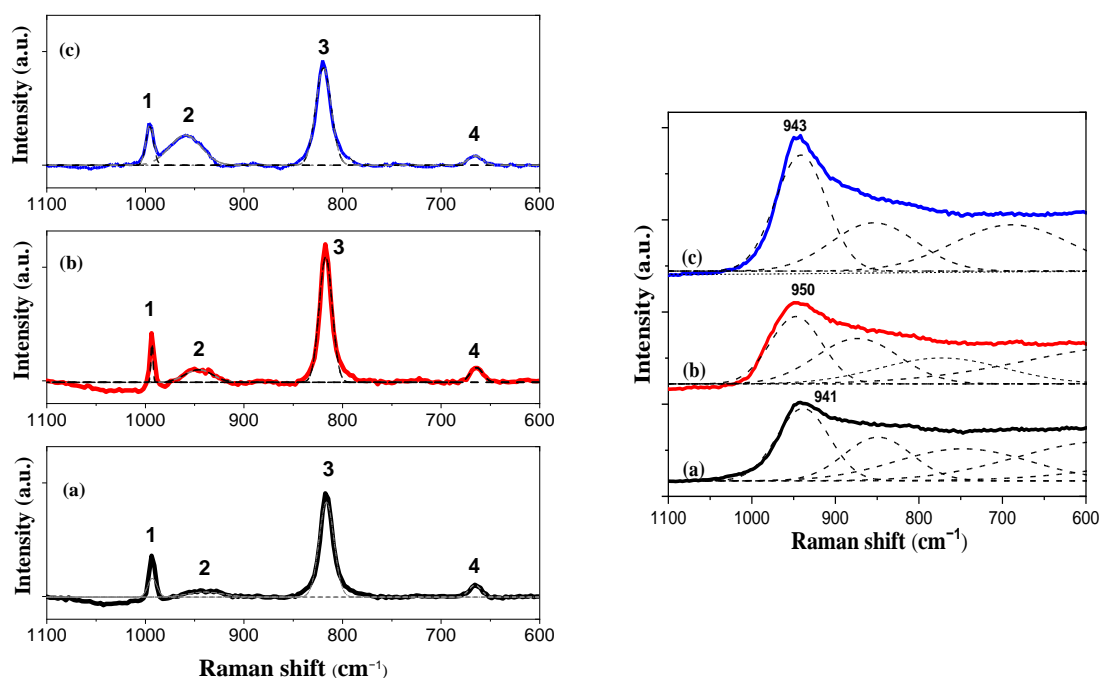


Figure 4. Raman Spectra for the Mo/AT2 (left) and CoMo/AT2 (right) catalysts by using different Mo loadings: (a) 10, (b) 12 and (c) 15 wt.%.

For the CoMo/AT2 catalyst, only one peak near 945 cm^{-1} is observed in all Mo loadings. A Gaussian deconvolution is needed to identify at least three more vibration signals. The intensity of the signal increased as a function of the Mo loading. This vibration signal is attributed to heptamolybdate species ($\text{Mo}_7\text{O}_{24}^{6-}$) elucidating the vibration of the terminal Mo=O bond [53,67,69]. However, the spectrum tail is attributed to overlapping between different surface species with similar vibrations. According to the literature [67,68], the vibrations of species along the tail are associated with the symmetric stretching of Mo-O and Co-O, which in turn relates to the formation of heptamolybdates and polymolybdates with the promotion of Co. Based on the intensity identified along the tail, the catalyst containing a Mo loading of 15 wt.% leads to a higher amount of the polyoxometalate species in accordance to DRS UV-vis and TPR results.

2.2. Catalytic Evaluation

Figure 5 exhibits the product yield and the initial reaction rate of the HDO of phenol with CoMoS/AT2 catalysts at different loadings of Mo and $\text{Co}/(\text{Co} + \text{Mo}) = 0.2$. It is possible to observe that the CoMo-based phase with a Mo loading of 12 wt.% shows approximately 2.3 times more activity than with a Mo loading of 10 wt.% and 1.5 times more than with 15 wt.%. The catalytic activity of these materials shows a volcano-like behavior where the catalyst with a Mo loading of 12 wt.% leads to the optimal performance of the catalyst. Concerning the selectivity, the main generated product via DDO is benzene; while products associated with HYD are cyclohexene and cyclohexane [10,40]. The catalyst with a Mo loading of 12 wt.% produces more benzene and less cyclohexane than the other two materials. This elucidates how the active sites of the MoS₂ slabs are well promoted by Co and generate a CoMoS II phase, which in turn provides enough CUS that favors DDO. Besides, the catalysts with a Mo loading of 10 and 15 wt.% lead to higher productions of cyclohexane and cyclohexene than the material with a Mo loading of 12 wt.%.

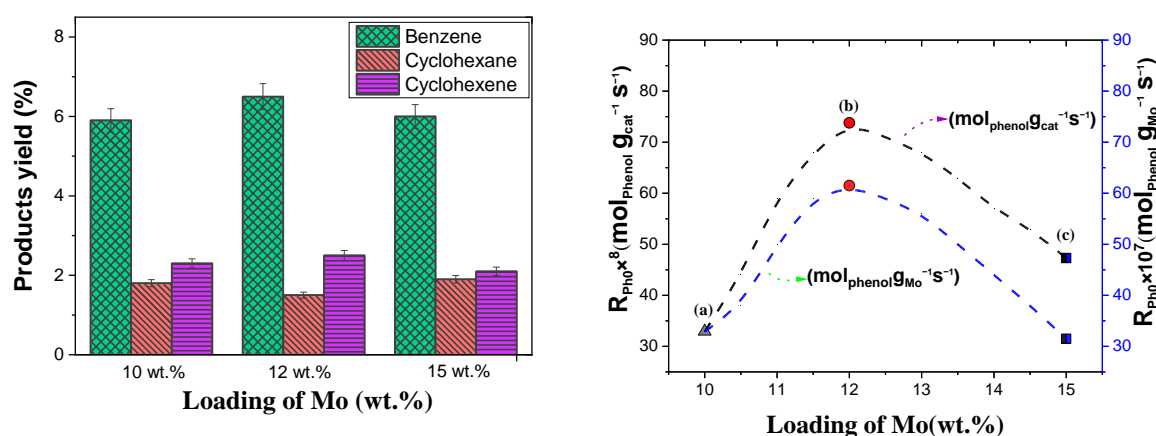


Figure 5. (Left) Products yield of the HDO of phenol over CoMoS/AT2 catalysts at 10% of conversion. (Right) Comparison of the initial reaction rates of CoMoS/AT2 with different Mo loadings at 320 °C and 5.5 MPa.

Figures 6 and 7 show the surface and contour response plots giving information on the effect of the operational pressure, the temperature and the Mo loading on the initial reaction rate and selectivity, see Equation (1), respectively. In general, the catalyst activity and selectivity are strongly affected by both the content of Mo and operational conditions. In particular, the maximum temperature (360 °C) and pressure (5.5 MPa) used during the experimentation leads to the highest activity of the CoMoS/AT2-based catalysts during their evaluation (see also Supplementary Materials Table S1). The optimal initial reaction rate of phenol over the CoMoS/AT2 catalyst is associated with a Mo loading of 12.5 wt.%; while the maximum selectivity is related to the catalyst with a Mo loading of 15 wt.%. On the contrary, those catalysts with a Mo loading of 10 and 15 wt.% lead to the minimum initial reaction rates, while the material with a Mo loading of 10 wt.% gives rise to the minimum selectivity. As expected from the previous analysis and the literature [32], independently of the catalyst, HYD is favored at lower temperatures, whereas DDO is favored at higher temperatures. In conclusion, the operating conditions leading to the optimal performance of CoMo/AT2 are 360 °C, 5.5 MPa, and a Mo loading of 12.5 wt.%.

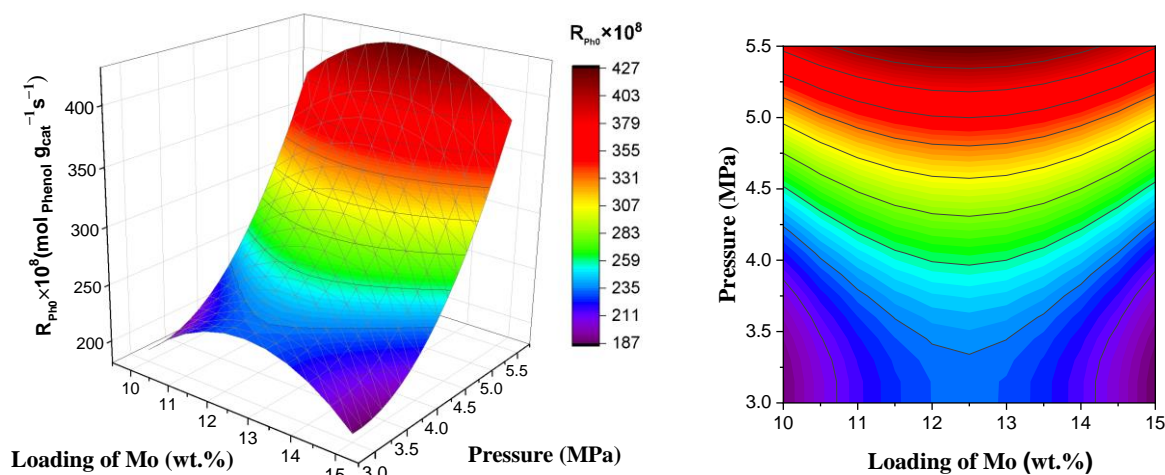


Figure 6. Response surface curve (left) and contour surface plot (right) corresponding to the initial reaction rate R_{PHO} of the HDO of phenol over CoMo/AT2 as a function of Mo loading (wt.%) and Pressure (MPa).

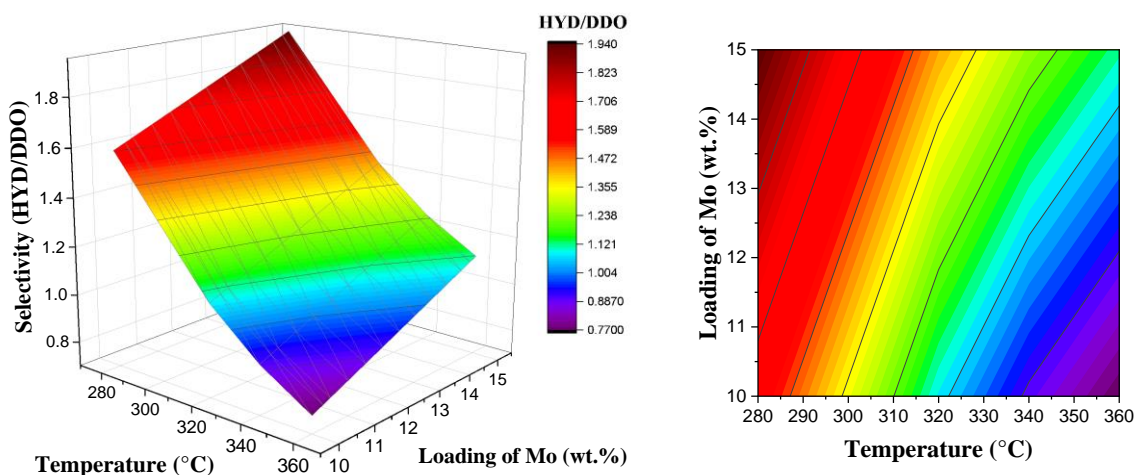


Figure 7. Response surface curve (left) and contour plot (right) correspond to selectivity as a function of Mo loading and temperature for the HDO of phenol over CoMo/AT2.

Since a Mo loading of 12 wt.% is the closest one to the Mo content (12.5 wt.%) leading to the optimal performance of the HDO of phenol, for this catalyst, Figure 8 elucidates the surface and contour response plots giving information on the effects of the operational temperature and total pressure on the route selectivity, while Table 1 summarizes the effect of temperature on the initial reaction of phenol and selectivity, at an operational pressure of 5.5 MPa. The highest operating temperature leads to the maximum initial reaction rate of phenol and the minimum selectivity [17]. Our experimental trends, associated with the effect of temperature and pressure on catalyst activity, have also been identified during the HDO of oxygenated-based molecules for CoMoS/AT2-based catalysts [48] and other catalysts [71].

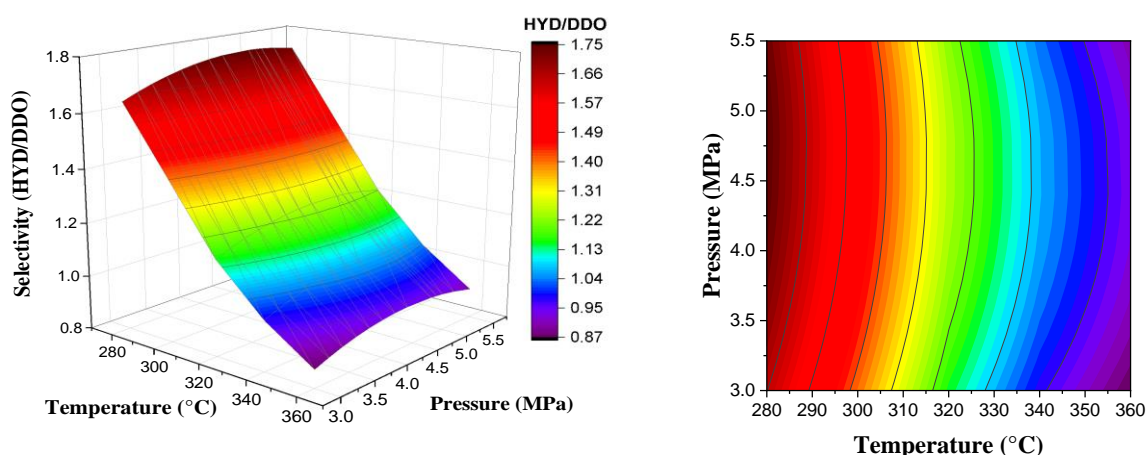


Figure 8. Response surface curve (left) and contour surface plot (right) correspond to the selectivity as a function of the reaction temperature and pressure for the HDO of phenol over a CoMo/AT2 material with a Mo loading of 12 wt.%.

Table 1. The effect of operational temperature on the initial reaction rate of phenol using a Co-MoS/AT2 material with a Mo loading of 12 wt.% and operational pressure of 5.5 MPa.

Temperature °C	$R_{Ph0} \times 10^8$ [mol _{Phenol} g _{cat} ⁻¹ s ⁻¹]	$R_{Ph0} \times 10^7$ [mol _{Phenol} g _{Mo} ⁻¹ s ⁻¹]	HYD/DDO
280	2.3	2.0	0.97
320	74	62	0.53
360	482	400	0.46

The statistical models for the responses are presented in Table 2. In these models, every response is influenced by operational conditions such as temperature (T), pressure (P), and Mo loading (C). The models are used to describe responses, as observed in Figures 6–8. Models follow a general second-order polynomial mathematical structure accounting for the operating conditions' linear, quadratic and two-way interactions on the responses. The coefficient located in the second, third, and fourth terms of the right-hand side of the models relates to the linear, quadratic, and two-way effects, respectively, while the first term is associated with the intercept. Although the coefficients in the models are empirical without physical sound, they provide quantitative information about the importance of every operating condition on the catalytic performance. The models contain 16 parameters, estimated via a non-linear regression, having as an input, 13 independent experiments (see Table S1 in Supplementary Materials). The analysis of variance (ANOVA) is presented in Table 3 to assess the suitability of the regression.

Table 2. Statistical model. Responses: Initial reaction rate of phenol R_{Ph0} and selectivity and Factors: Temperature (T, °C), Pressure (P, MPa) and Mo loading (C, wt.%) and their respective correlation coefficients.

Model	R^2 (%)
$R_{Ph0} = 7.42 \times 10^{-2} - 4.83 \times 10^{-4}(T) - 6.57 \times 10^{-3}(P) + 1.75 \times 10^{-3}(C) + 7.257 \times 10^{-7}(T^2) + 3.28 \times 10^{-4}(P^2) - 7.02 \times 10^{-5}(C^2) + 1.26 \times 10^{-5}(T \cdot P)$	91.9
$S = 8.93 - 4.88 \times 10^{-2}(T) + 3.99 \times 10^{-1}(P) + 6.6 \times 10^{-2}(C) + 6.2155 \times 10^{-5}(T^2) - 3.57 \times 10^{-2}(P^2) - 1.38 \times 10^{-4}(C^2) + 2.19 \times 10^{-4}(T \cdot P)$	97.1

Table 3. Analysis of variance (ANOVA) for second-order models (95% probability).

Source	D. F. *	Sum of Squares	Mean Square	F-Value	p-Value
Model of Activity (R_{Ph0})					
Regression	7	2.3×10^{-5}	3.0×10^{-6}	8.16	0.017
Linear effect	3	1.6×10^{-5}	6.0×10^{-6}	13.78	0.007
Quadratic effect	3	6.0×10^{-6}	2.0×10^{-6}	4.65	0.066
Interaction effect	1	2.0×10^{-6}	2.0×10^{-6}	4.04	0.101
Residual error	5	2.0×10^{-6}	22.0×10^{-7}		
Total	12	2.5×10^{-5}			
Model of Selectivity (S)					
Regression	6	6.95×10^{-0}	1.159×10^{-1}	33.38	0.001
Linear effect	3	6.45×10^{-1}	2.1×10^{-1}	60.42	0.001
Quadratic effect	2	4.87×10^{-2}	2.43×10^{-2}	7.02	0.027
Interaction effect	1	1.98×10^{-3}	1.98×10^{-3}	0.57	0.478
Residual error	6	2.08×10^{-2}			
Total	12	7.16×10^{-1}			

* Degree of freedom.

The surface and contour plots exhibit curvatures that can be considered reliable considering the structure of the models and the experimental design implemented in this work. The coefficient of determination (R^2) is 0.91 for the initial reaction rate and 0.97 for the selectivity, meaning that the model is adequate. However, the F-value for the initial reaction rate and the selectivity is higher than the tabulated one, while the p -value for two responses is lower than 0.5. These statistical results elucidate how the statistical models both describe observations correctly and adequately account for the operating conditions' effect on the initial reaction rate and selectivity.

The coefficients estimated for the model that describes the initial reaction rate suggest that the linear, quadratic, and interaction effects affect this response such that their F-value was higher than the tabulated one (2.3) and their p -value is lower than 0.5. Analyzing their magnitude order, the interaction effect between pairs of factors is the one with a minimum impact on the response. In contrast, the linear effect leads to a stronger influence on the response.

Moreover, based on the estimated values of the coefficients for the selectivity model, the F-value and p -value suggest that linear and quadratic effects are the main factors impacting the response such that their F-value is higher than the tabulated one and their p -value is lower than 0.5. Nevertheless, the interaction effect presents the minimum statistical impact on the response such that the F-value is higher than the tabulated one and the p -value is slightly lower than 0.5. Thus, the three factors, Mo loading, temperature and pressure, impact both the initial reaction rate and selectivity.

3. Discussion

The results have proved that CoMoS/Al₂O₃-TiO₂ is a promising catalyst for the HDO of oxygenated-based molecules [17,20,25]. Nevertheless, its application at large reactor scales needs different catalytic and kinetic analyses that allow a deeper understanding of its catalytic surface and, hence, its improvement. According to our results and literature findings [25,48,50], Co and Mo surface species in the active phase and their interaction with the support significantly impact the activity and selectivity of the CoMoS/Al₂O₃-TiO₂ catalyst. First, previous studies evaluating the effect of the Al/Ti atomic ratio in the Al₂O₃-TiO₂ mixed oxide on the performance of the CoMoS active phase identified how an

Al/Ti = 2 (AT2) increased the catalytic activity significantly in the HDO of phenol [48,54]. When compared with the state-of-the-art CoMoS/Al₂O₃ catalyst, the use of AT2 increases Mo^{oh} and Co^{oh} species, which were associated with a higher formation of active sites for both the HYD and DDO during the HDO of oxygenated-based molecules. For instance, the increase in Co^{oh} species led to higher availability of MoS₂ slabs during the corresponding sulfidation of the CoMo/AT2 catalyst, explaining the promoting activity and less inhibition of its catalytic surface during the HDO of phenol [25,48]. Second, studies assessing the impact of the Co/(Co + Mo) ratio were carried out to identify its impact on the HDO of oxygenated-based molecules over a CoMoS/AT2 catalyst [25]. Their observations suggested how a Co/(Co + Mo) = 0.2 led to a higher activity at the operating conditions studied during the HDO of phenol. Catalyst activity and selectivity were associated with the qualitative formation of Mo^{oh} and Co^{oh} species in the active phase. At the same time, the yield to the different species was insensitive to the Co/(Co + Mo) ratio. In this regard, Co^{oh} species were related to the formation of a high content of the CoMoS phase, which promoted the formation of active sites and, hence, the catalyst activity [25]. Thus, although the previous research elucidated how the activity was improved, it was not possible to identify the Mo loading and operating conditions leading to the optimization of the performance for the CoMoS/AT2 catalyst, using a Co/(Co + Mo) = 0.2, during the HDO of phenol.

To the above end, because of the promising results of the CoMoS/AT2 catalyst, our research focused on finding the optimal catalytic and kinetic performance of this material and relating it to the formation of Co and Mo surface species when varying the Mo loading. As engineering methodology to identify the optimal performance of the catalyst, an RSM, based on the Box–Behnken experimental design, was applied accordingly. In what follows, the main discussion of our results is presented. First, different from what was identified in the literature [48], the best catalytic performance is identified when using a Mo loading of 12.5 wt.% rather than 15 wt.% in the CoMoS active phase. The catalytic results are associated with the formation of Mo and Co species in the active phase. Table 4 gives quantitative information on their generation when varying the Mo loading in the CoMo/AT2 catalyst. Regarding (Co + Mo)^{oh}, (Co + Mo)th and Ti⁴⁺ species, the highest value is identified for the material with a Mo loading of 15 wt.%, while the lowest one is associated with a Mo loading of 10 wt.%, also agreeing with the literature [48,65]. Second, it is observed that the formation of (Co + Mo)^{oh,th} species in the active phase of the evaluated catalysts is favored when the catalyst contains a Mo loading of 12 wt.%. Particularly, it is worth stressing that the (Co + Mo)^{oh}/(Co + Mo)th ratio does not follow a conventional trend such that its lowest value is obtained with a Mo loading of 12 wt.%, while the highest value is associated with a Mo loading of 10 wt.%. In this regard, Figure 9 displays how the initial reaction rate of phenol relates to the (Co + Mo)^{oh}/(Co + Mo)th ratio when the CoMoS/AT2 materials are evaluated at 320 °C and 5.5 MPa. Different from what was reported in the literature [48], the most active CoMoS/AT2 material is not the one with the highest Mo loading or with the highest concentration of Co^{oh} and Mo^{oh} species but the one (Mo loading of 12 wt.%) with the lowest (Co + Mo)^{oh}/(Co + Mo)th ratio. Therefore, the catalyst activity is associated with a combination between (Co + Mo)^{oh} and (Co + Mo)th species, such that the catalyst presenting the lowest (Co + Mo)^{oh}/(Co + Mo)th ratio also gives rise to the highest catalyst activity. Regarding the yield of the different products, the active phase with Mo loading of 12 wt.% follows trends as in the other catalytic materials, where DDO, leading to the formation of benzene, is favored over HYD leading, to the formation of cyclohexene. Note, in Figure 9, that the higher the conversion of phenol is, the higher the production of cyclohexane out of cyclohexene becomes.

Table 4. H₂ consumption for Co and Mo species involved in the CoMo/AT2 using different loadings of Mo: 10, 12 and 15 wt.%.

Mo Loading [wt.%]		(Co + Mo) ^{oh} (400–550 °C)	(Co + Mo) ^{oh,th} (550–650 °C)	(Co + Mo) th (650–750 °C)	Ti ⁴⁺ (≥750 °C)	(Co + Mo) ^{oh} / (Co + Mo) th
10	T (°C)	497	599	700	832	0.77
	H ₂ *	123.21	55.47	159.25	83.91	
12	T (°C)	482	590	712	856	0.48
	H ₂ *	133.82	76.04	273.04	147.49	
15	T (°C)	467	557	681	841	0.6
	H ₂ *	195.52	54.66	323.84	150.61	

* H₂ relative consumption associated with TPR profiles [$\mu\text{mol/gcat}$].

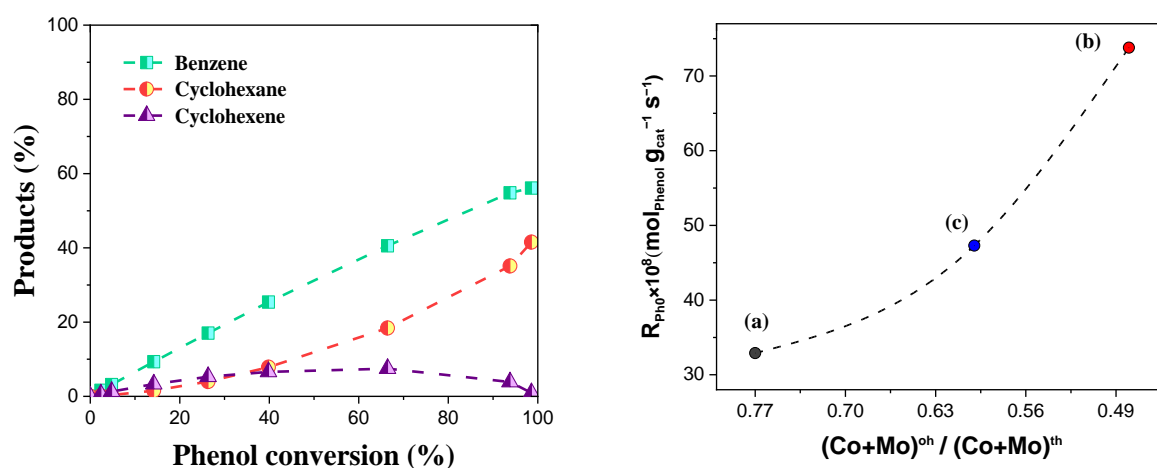


Figure 9. Distribution of products with respect to phenol conversion (left) and correlation between the in-ital reaction rate and Co and Mo species (right) during the HDO of phenol over a CoMoS/AT2 catalyst using different loading of Mo: (a) 10, (b) 12 and (c) 15 wt.%. Operating conditions: 320 °C and 5.5 MPa.

Complementing the above discussion, when the Mo loading is 10 wt.%, strong metal-support interactions generate more Moth and Coth than octahedral species; this is, probably, associated with less sulfidation in the active phase because of the possible formation of CoMoO₄, as TPR results suggest. On the other hand, Co promoted the formation of MoS₂ to a lower extent for Mo loadings of 12 and 15 wt.% resulting mainly in the selective formation of the CoMoS phase. Regarding the catalyst with a Mo loading of 15 wt.%, as it contains more Mo and Co in the active phase, the formed MoS₂ slabs presented less edge Mo, increasing HYD but decreasing the catalyst activity. Therefore, it is possible to confirm that the CoMoS phase with a Mo loading of 12 wt.% generates a higher concentration of active sites because due to its adequate concentration of Mo and Co on the surface, when compared with those catalysts with Mo loadings of 10 and 15 wt.%.

Finally, Table 5 shows the contribution analysis and initial reaction rates for DDO and HYD during the HDO of phenol over the CoMoS/AT2 catalysts with a Mo loading of 10, 12, and 15%. These catalyst responses are calculated when the reaction takes place at 320 °C and 5.5 MPa. Additionally, Figure 10 summarizes the reaction scheme following the formation of the different byproducts via DDO and HYD. This figure also presents contributing factors identified for the catalysts presenting the lowest (Co + Mo)^{oh} / (Co + Mo)th ratio, i.e., a Mo loading of 12 wt.%. As mentioned earlier, the proposal of the reaction scheme collects all observations obtained at different Mo loadings and operating conditions assessed in this contribution. So far, the results presented herein agree with those identified in Section 2.2, such that a Mo loading of 12 wt.% leads to the higher initial reaction rates of

both DDO and HYD compared with those active phases using different Mo loadings. This kinetic result is corroborated when analyzing the contributing factors which do indicate that the highest contributing factor relates to the DDO route followed by HYD1, HYD4 and HYD5, agreeing with the analysis of product yields presented in Figure 9. Contributing factors do elucidate the stability of benzene to not react and produce cyclohexane at the studied operating conditions.

Table 5. Contribution factors for phenol HDO products in CoMoS/AT2 catalysts with Mo loadings of 10, 12 and 15 wt.%. Operating conditions: 320 °C and 5.5 MPa.

Catalysts (wt.% de Mo)	10	12	15
RDDO[molPhenol/gcat s] × 108	18.6 ± 2	49.7 ± 3	31.5 ± 33
RHYD1[molPhenol/gcat s] × 108	7.7 ± 1	20.4 ± 2	12 ± 1
RHYD4[molPhenol/gcat s] × 108	6.8 ± 1	5.3 ± 1	5 ± 1
$\varphi_{DDO}(\%)$	56	65	64
$\varphi_{HYD1}(\%) = \varphi_{HYD3}(\%)$	23	27	24
$\varphi_{HYD4}(\%)$	15	6.4	9.5
$\varphi_{HYD5}(\%)$	5	0.6	1.5

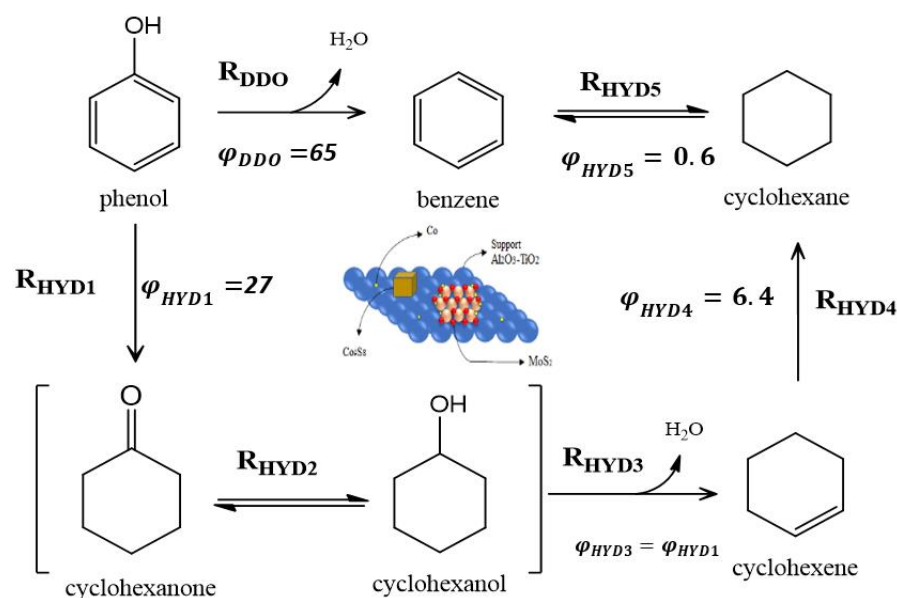


Figure 10. Reaction scheme and contribution analysis obtained for the CoMoS/AT2 catalyst with a Mo loading of 12 wt.% when this mixed oxide is evaluated during the HDO of phenol at 320 °C and 5.5 MPa. Contribution factor is obtained for a Mo loading of 12 wt.%.

4. Methodology

4.1. Catalyst Synthesis

The support based on a Al₂O₃-TiO₂ oxide with an Al/Ti = 2 (AT2) was synthesized following the sol-gel method, as described elsewhere [25]. As precursors, tri-sec-butoxide (Al (OCH(CH₃) C₂H₅)₃; Aldrich 99.9%, St. Louis, MI, USA) and titanium isopropoxide (Ti (OCH₂CH₂)₄; Aldrich 98%, St. Louis, MI, USA) were used. Thus, 2-propanol (CH₃)₂CHOH; Baker 99.5%, Ecatepec, Estado de Mexico, Mexico) and nitric acid (HNO₃; Baker 99.5%, Ecatepec, Estado de Mexico, Mexico) were used as solvent and as hydrolysis catalyst. The nominal molar ratio implemented for the preparation of the support was 2-propanol/alkoxide = 65, H₂O/alkoxide = 20 HNO₃/alkoxide = 0.2, aluminum/titanium = 2 [48]. Thus, 2-propanol was cooled to 4 °C and under vigorous

stirring, the theoretical amounts of Al and Ti were added. Then, HNO₃ aqueous solution was added slowly dropwise. The obtained gel was aged for 24 h at normal conditions. Subsequently, it was placed in a crystallizer at 65 °C in a water bath to evaporate the liquids. The supports obtained were calcined at 500 °C for 3 h under an air atmosphere. Finally, between 80 and 100 mesh (0.177–0.149 mm) were ground and sifted. AT2 was, subsequently, impregnated by the impregnation method using an aqueous solution of ammonium heptamolybdate ((NH₄)₆Mo₇O₂₄·4H₂O; Aldrich 99.9%, St. Louis, MI, USA) and cobalt nitrate ((Co(NO₃)₂·6H₂O; Aldrich 99%, St. Louis, MI, USA). The Mo/AT2 and CoMo/AT2 series were synthesized with the following Mo loadings: 10, 12, and 15 wt.%. The CoMo-based series were impregnated following a Co/(Co + Mo) molar ratio of 0.2. For the Mo/AT2, the solution was maintained at room conditions for 12 h. After that, it was dried at 120 °C and calcinated at 400 °C for 5 h. For the CoMo/AT2, the Mo/AT2 materials were impregnated with the cobalt solution and the heat treatment was repeated.

4.2. Catalysts Characterization

N₂ Physisorption. The AT2 support was characterized in a gas sorption instrument, model Autosorb iQ brand Quantachrome (Boynton Beach, FL, USA) Lab. ISASA. The sample was degassed at 150 °C in vacuum for 8 h with ultra-high purity Nitrogen (<99.999% or 5.0). The specific area was determined by the Brunauer-Emmett-Teller (BET) multi-point method in a relative pressure interval of (P/P₀) (0.05 to 0.25). The pore diameter was determined by the Barret-Joyner-Hallender (BJH) method.

X-Ray Diffraction (XRD). The XRD pattern of AT2 support was performed in a BRUKER D-8 ADVANCE diffractometer with Bragg geometry: Brentthane θ - θ , Cu K α radiation, Ni 0.5% Cu-K β filter in the secondary beam and a position-sensitive one-dimensional silicon strip detector (Bruker, Lynxeye, Billerica, MA, USA). The intensity of the diffraction as a function of the angle 2θ was measured between 4 and 80°, with a step of 0.02° per 0.5 s per point.

UV-vis diffuse reflectance spectra (DRS UV-vis). The DRS UV-vis spectra (Labsphere RSA-PE-20, North Sutton, NH, USA) were measured in the range of 200 to 1000 nm at room temperature with a PERKIN ELMER LAMBDA 35 spectrometer equipped with an integration sphere (LABSPHERE RSA-PE-20). The samples were sieved until obtaining 100 mesh (<150 μ m), and dried at 393 K for 2 h. The spectra were measured in the reflectance mode considering an infinite thickness (R_{∞}) using the reflectance of MgO as a reference. Data acquisition was in the 0.5 nm range with a scan speed of 240 nm/min.

Thermo-programmed reduction (TPR). TPR experiments were carried out in an AMI-80 system equipped with a thermal conductivity detector (TCD) (Pittsburgh, PA, USA). The sample (100 mg) was loaded in the quartz U cell and prepared in-situ at 523 K for one h under a flow of 35 mL/min of He. The temperature was raised with a heating ramp of 15 °C/min from room temperature to 900 °C, under a constant stream of 50 mL/min of H₂/Ar at 10 vol.%.

Raman spectroscopy. Laser Raman spectroscopy (LRS) was analyzed with a Perkin Elmer GX Raman FT-IR (Waltham, MA, USA), equipped with an Nd: YAG (1064 nm) laser and InGaAs detector. The data acquisition was carried out with a laser power of 40 to 300 mW at the 3600 to 100 cm⁻¹ Raman shift range with a resolution of 2 to 4 cm⁻¹.

4.3. Catalytic Evaluation

Experimentation was carried out in a batch reactor (Parr model 5500). The feedstock contained a solution of 100 mL of phenol dissolved in hexadecane. The concentration of oxygen in this solution was equal to 500 ppm (or 2223 ppm of phenol). The reactor operated with 0.1 g of a sulfided catalyst with a mesh ranging from 80 to 100 (<150 μ m). It is worth mentioning that this mesh led to minimizing intraparticle transport resistances [25,48,56]. To this end, the reaction was initiated, once the system was agitated at 1000 rpm. This agitation rate led to minimize interparticle transport resistances [25,48,56]. The catalyst was activated ex situ with a flow of H₂S/H₂ at 15% v/v at 400 °C for 2 h. Because phenol is

in the solid phase at normal temperature and pressure conditions, a study of solubility and phase equilibrium between phenol and different solvents was previously carried out [56], and it was identified that hexadecane was one of the molecules where phenol presented higher solubility.

The experimental design was based on the well-known response surface method (RSM) [72]. Three factors (Temperature, pressure, and Mo loading) and three levels (−1, 0, 1) were selected to follow the Box–Behnken design, see Table 6. The response variables are the catalyst activity R_{Ph0} (initial reaction rate) and the selectivity S .

Table 6. Coded levels of experiments involved in the Box–Behnken design.

Level B-BD	Pressure (MPa)	Temperature (°C)	Load of Metal (wt/wt.%)
−1	3	280	10
0	4	320	12
1	5.5	360	15

The reaction's products were analyzed using a Shimadzu GC 2010 Plus gas chromatograph with an AOC-20i automatic injection bridge, equipped with an Agilent CP-Sil5 CB 60 m × 0.32 mm × 1.0 μm column and a flame ionization detector (FID). Subsequently, the conversions and yields were determined using a proper calibration curve based on the area under the curve of the products analyzed in the gas chromatograph. Selectivity was determined with a relationship between the products of the HYD hydrogenation pathway (cyclohexene and cyclohexane) and the compound (benzene) associated with the DDO pathway, as shown in Equation (1).

$$S = \frac{\text{HYD}}{\text{DDO}} \quad (1)$$

4.4. Contribution Analysis

To evaluate the impact of the global reaction steps of HDO, a contribution analysis was carried out using contribution factors determined by reaction rates integrated over time.

$$\varphi_{i,j} = \frac{r_{ij}}{\sum r_{ij}} \quad (2)$$

where, $\varphi_{i,j}$ is the integral contribution factor that for the reaction step i accounts for the appearance/disappearance of the component j . It is generally defined as the ratio of the rate of appearance/disappearance of j resulting from the reaction i to the total rate of appearance/disappearance of j inside the reactor.

5. Conclusions

This work evaluated the HDO of phenol over a CoMoS supported on Al₂O₃-TiO₂ mixed oxide with an Al/Ti = 2 (AT2) and Co/(Co + Mo) = 0.2. The optimization of the catalytic performance of HDO followed an RSM using a Box–Behnken experimental design. Based on the development of a statistical model, it was elucidated how the initial reaction rate and selectivity depend closely on three established factors: Mo loading (10–15 wt.%), temperature (280–360 °C), and pressure (3–5.5 MPa). The responses were slightly affected by the interaction between any pair of factors, while the linear and quadratic effects of the operating conditions and Mo loading strongly influenced the responses. The CoMo/AT2 catalyst achieved the optimal catalytic performance with a Mo loading of 12.5 wt.%, a temperature of 360 °C, and a system total pressure of 5.5 MPa. The highest pressure favored the presence of hydrogen in the liquid media, overcoming thermodynamic limitations. However, high temperature kinetically increased the reaction rate according to the transition state theory. As a relevant finding of this contribution, the lowest Mo loading presented the lowest (Co + Mo)^{oh}/(Co + Mo)th ratio, which favored the formation of active sites

for HYD and DDO. Nevertheless, the DDO was always predominant under all studied operating conditions.

Since this study determined the operational conditions leading to the optimal performance of the HDO over CoMoS/AT2, future research will evaluate the kinetic performance and changes in the catalyst's surface and structure around the optimal conditions. The kinetic analysis will rest on proposing an elemental reaction mechanism and developing a kinetic model, while the study of the catalyst surface will depend on its appropriate characterization through the operation time, from the start-up to the shut-off of the experiment. Thus, their output will be associated, such that after it, the kinetic and catalyst deactivation analyses will pave the way for the future application of the CoMoS/AT2 during the HDO of different oxygenated-based molecules in different reactor operation modes and scales.

Supplementary Materials: The following supporting information can be downloaded at: <https://www.mdpi.com/article/10.3390/catal12101139/s1>, Table S1: Raw data obtained by following the RSM by using the Box–Behnken experimental design.

Author Contributions: Conceptualization, J.A.d.l.R. and C.O.C.-A.; Formal analysis, I.P.-R., C.O.C.-A. and J.A.T.-P.; Investigation, I.P.-R., C.O.C.-A. and J.A.d.l.R.; Methodology, C.O.C.-A. and I.P.-R.; Project administration, J.A.d.l.R.; Resources, J.A.d.l.R.; Software, C.O.C.-A.; Supervision, C.O.C.-A. and J.A.d.l.R.; Visualization, J.A.T.-P. and, I.P.-R.; Writing—original draft, I.P.-R. and C.O.C.-A.; Writing—review & editing, J.A.T.-P., J.A.d.l.R. and C.O.C.-A.. All authors have read and agreed to the published version of the manuscript.

Funding: The authors express their gratitude to CONACYT (Mexico) for financial support through the project funding: A1-S-41193. I.P.-R. is grateful for the master fellowship CONACyT-SENER with number 471763 and doctoral fellowship from CONACyT with scholarship number 704465.

Data Availability Statement: The data presented in this study are available through the manuscript and in Supplementary Materials.

Conflicts of Interest: The authors declare no conflict of interest.

References

1. Ding, S.; Parlett, C.M.A.; Fan, X. Recent developments in multifunctional catalysts for fatty acid hydrodeoxygenation as a route towards biofuels. *Mol. Catal.* **2022**, *523*, 111492. [[CrossRef](#)]
2. Valle, B.; Remiro, A.; García-Gómez, N.; Gayubo, A.G.; Bilbao, J. Recent research progress on bio-oil conversion into bio-fuels and raw chemicals: A review. *J. Chem. Technol. Biotechnol.* **2019**, *94*, 670–689. [[CrossRef](#)]
3. Ambursa, M.M.; Juan, J.C.; Yahaya, Y.; Taufiq-Yap, Y.H.; Lin, Y.C.; Lee, H.V. A review on catalytic hydrodeoxygenation of lignin to transportation fuels by using nickel-based catalysts. *Renew. Sustain. Energy Rev.* **2021**, *138*, 110667. [[CrossRef](#)]
4. Dabros, T.M.H.; Stummann, M.Z.; Høj, M.; Jensen, P.A.; Grunwaldt, J.D.; Gabrielsen, J.; Mortensen, P.M.; Jensen, A.D. Transportation fuels from biomass fast pyrolysis, catalytic hydrodeoxygenation, and catalytic fast hydroxypropylation. *Progress Energy Combust. Sci.* **2018**, *68*, 268–309. [[CrossRef](#)]
5. Pourzolfaghar, H.; Abnisa, F.; Wan Daud, W.M.A.; Aroua, M.K. Atmospheric hydrodeoxygenation of bio-oil oxygenated model compounds: A review. *J. Anal. Appl. Pyrolysis* **2018**, *133*, 117–127. [[CrossRef](#)]
6. Li, X.; Chen, G.; Liu, C.; Ma, W.; Yan, B.; Zhang, J. Hydrodeoxygenation of lignin-derived bio-oil using molecular sieves supported metal catalysts: A critical review. *Renew. Sustain. Energy Rev.* **2017**, *71*, 296–308. [[CrossRef](#)]
7. Zhao, C.; Kou, Y.; Lemonidou, A.A.; Li, X.; Lercher, J.A. Highly Selective Catalytic Conversion of Phenolic Bio-Oil to Alkanes. *Angew. Chem.* **2009**, *48*, 3987–3990. [[CrossRef](#)]
8. Patel, M.; Kumar, A. Production of renewable diesel through the hydroprocessing of lignocellulosic biomass-derived bio-oil: A review. *Renew. Sustain. Energy Rev.* **2016**, *58*, 1293–1307. [[CrossRef](#)]
9. Gutierrez, A.; Turpeinen, E.M.; Viljava, T.R.; Krause, O. Hydrodeoxygenation of model compounds on sulfided CoMo/γ-Al₂O₃ and NiMo/γ-Al₂O₃ catalysts; Role of sulfur-containing groups in reaction networks. *Catal. Today* **2017**, *285*, 125–134. [[CrossRef](#)]
10. Ryymin, E.M.; Honkela, M.L.; Viljava, T.R.; Krause, A.O.I. Competitive reactions and mechanisms in the simultaneous HDO of phenol and methyl heptanoate over sulphided NiMo/γ-Al₂O₃. *Appl. Catal. A Gen.* **2010**, *389*, 114–121. [[CrossRef](#)]
11. Yoosuk, B.; Tumnantong, D.; Prasassarakich, P. Unsupported MoS₂ and CoMoS₂ catalysts for hydrodeoxygenation of phenol. *Chem. Eng. Sci.* **2012**, *79*, 1–7. [[CrossRef](#)]
12. Nimmanwudipong, T.; Runnebaum, R.C.; Block, D.E.; Gates, B.C. Catalytic conversion of guaiacol catalyzed by platinum supported on alumina: Reaction network including hydrodeoxygenation reactions. *Energy Fuels* **2011**, *25*, 3417–3427. [[CrossRef](#)]

13. Echeandia, S.; Arias, P.L.; Barrio, V.L.; Pawelec, B.; Fierro, J.L.G. Synergy effect in the HDO of phenol over Ni-W catalysts supported on active carbon: Effect of tungsten precursors. *Appl. Catal. B* **2010**, *101*, 1–12. [\[CrossRef\]](#)
14. Wildschut, J.; Mahfud, F.H.; Venderbosch, R.H.; Heeres, H.J. Hydrotreatment of fast pyrolysis oil using heterogeneous noble-metal catalysts. *Ind. Eng. Chem. Res.* **2009**, *48*, 10324–10334. [\[CrossRef\]](#)
15. Yang, Y.; Gilbert, A.; Xu, C. Hydrodeoxygenation of bio-crude in supercritical hexane with sulfided CoMo and CoMoP catalysts supported on MgO: A model compound study using phenol. *Appl. Catal. A Gen.* **2009**, *360*, 242–249. [\[CrossRef\]](#)
16. Bui, V.N.; Laurenti, D.; Afanasiev, P.; Geantet, C. Hydrodeoxygenation of guaiacol with CoMo catalysts. Part I: Promoting effect of cobalt on HDO selectivity and activity. *Appl. Catal. B* **2011**, *101*, 239–245. [\[CrossRef\]](#)
17. Bui, V.N.; Laurenti, D.; Delichère, P.; Geantet, C. Hydrodeoxygenation of guaiacol. Part II: Support effect for CoMoS catalysts on HDO activity and selectivity. *Appl. Catal. B* **2011**, *101*, 246–255. [\[CrossRef\]](#)
18. Ryymin, E.M.; Honkela, M.L.; Viljava, T.R.; Krause, A.O.I. Insight to sulfur species in the hydrodeoxygenation of aliphatic esters over sulfided NiMo/ γ -Al₂O₃ catalyst. *Appl. Catal. A Gen.* **2009**, *358*, 42–48. [\[CrossRef\]](#)
19. Grilc, M.; Likozar, B.; Levec, J. Hydrotreatment of solvolytically liquefied lignocellulosic biomass over NiMo/Al₂O₃ catalyst: Reaction mechanism, hydrodeoxygenation kinetics and mass transfer model based on FTIR. *Biomass Bioenergy* **2014**, *63*, 300–312. [\[CrossRef\]](#)
20. Dugulan, A.I.; van Veen, J.A.R.; Hensen, E.J.M. On the structure and hydrotreating performance of carbon-supported CoMo- and NiMo-sulfides. *Appl. Catal. B* **2013**, *142–143*, 178–186. [\[CrossRef\]](#)
21. Ojagh, H.; Creaser, D.; Tamm, S.; Arora, P.; Nyström, S.; Lind Grennfelt, E.; Olsson, L. Effect of Dimethyl Disulfide on Activity of NiMo Based Catalysts Used in Hydrodeoxygenation of Oleic Acid. *Ind. Eng. Chem. Res.* **2017**, *56*, 5547–5557. [\[CrossRef\]](#)
22. Lin, Y.C.; Li, C.L.; Wan, H.P.; Lee, H.T.; Liu, C.F. Catalytic hydrodeoxygenation of guaiacol on Rh-based and sulfided CoMo and NiMo catalysts. *Energy Fuels* **2011**, *25*, 890–896. [\[CrossRef\]](#)
23. Sun, M.; Adjaye, J.; Nelson, A.E. Theoretical investigations of the structures and properties of molybdenum-based sulfide catalysts. *Appl. Catal. A Gen.* **2004**, *263*, 131–143. [\[CrossRef\]](#)
24. Escobar, J.; de Los Reyes, J.A.; Viveros, T. Nickel on TiO₂-modified Al₂O₃ sol-gel oxides: Effect of synthesis parameters on the supported phase properties. *Appl. Catal. A Gen.* **2003**, *253*, 151–163. [\[CrossRef\]](#)
25. Tavizón-Pozos, J.A.; Suárez-Toriello, V.A.; del Ángel, P.; de Los Reyes Heredia, J.A. Hydrodeoxygenation of Phenol over Sulfided CoMo Catalysts Supported on a Mixed Al₂O₃-TiO₂ Oxide. *Int. J. Chem. React. Eng.* **2016**, *14*, 1211–1223. [\[CrossRef\]](#)
26. García-Martínez, J.C.; Castillo-Araiza, C.O.; de los Reyes Heredia, J.A.; Trejo, E.; Montesinos, A. Kinetics of HDS and of the inhibitory effect of quinoline on HDS of 4,6-DMDBT over a Ni-Mo-P/Al₂O₃ catalyst: Part I. *Chem. Eng. J.* **2012**, *210*, 53–62. [\[CrossRef\]](#)
27. Wei, S.; Wang, F.; Dan, M.; Zeng, K.; Zhou, Y. The role of high oxygen vacancy concentration on modification of surface properties and H₂S adsorption on the rutile TiO₂ (110). *Appl. Surf. Sci.* **2017**, *422*, 990–996. [\[CrossRef\]](#)
28. Popov, A.; Kondratieva, E.; Goupil, J.M.; Mariey, L.; Bazin, P.; Gilson, J.P.; Travert, A.; Mauge, F. Bio-oils hydrodeoxygenation: Adsorption of phenolic molecules on oxidic catalyst supports. *J. Phys. Chem. C* **2010**, *114*, 15661–15670. [\[CrossRef\]](#)
29. Popov, A.; Kondratieva, E.; Mariey, L.; Goupil, J.M.; el Fallah, J.; Gilson, J.P.; Travert, A.; Mauge, F. Bio-oil hydrodeoxygenation: Adsorption of phenolic compounds on sulfided (Co)Mo catalysts. *J. Catal.* **2013**, *297*, 176–186. [\[CrossRef\]](#)
30. Sharifvaghefi, S.; Yang, B.; Zheng, Y. New insights on the role of H₂S and sulfur vacancies on dibenzothiophene hydrodesulfurization over MoS₂ edges. *Appl. Catal. A Gen.* **2018**, *566*, 164–173. [\[CrossRef\]](#)
31. Kibsgaard, J.; Tuxen, A.; Knudsen, K.G.; Brorson, M.; Topsøe, H.; Lægsgaard, E.; Lauritsen, J.V.; Besenbacher, F. Comparative atomic-scale analysis of promotional effects by late 3d-transition metals in MoS₂ hydrotreating catalysts. *J. Catal.* **2010**, *272*, 195–203. [\[CrossRef\]](#)
32. Zhao, Y.P.; Wu, F.P.; Song, Q.L.; Fan, X.; Jin, L.J.; Wang, R.Y.; Cao, J.P.; Wei, X.Y. Hydrodeoxygenation of lignin model compounds to alkanes over Pd–Ni/HZSM-5 catalysts. *J. Energy Inst.* **2020**, *93*, 899–910. [\[CrossRef\]](#)
33. Rios-Escobedo, R.; Ortiz-Santos, E.; Colín-Luna, J.A.; Díaz de León, J.N.; Escobar, P.A.J.; de los Reyes Heredia, J.A. Anisole Hydrodeoxygenation: A Comparative Study of Ni/TiO₂-ZrO₂ and Commercial TiO₂ Supported Ni and NiRu Catalysts. *Top. Catal.* **2022**, *65*, 1448–1461. [\[CrossRef\]](#)
34. He, Y.; Bie, Y.; Lehtonen, J.; Liu, R.; Cai, J. Hydrodeoxygenation of guaiacol as a model compound of lignin-derived pyrolysis bio-oil over zirconia-supported Rh catalyst: Process optimization and reaction kinetics. *Fuel* **2019**, *239*, 1015–1027. [\[CrossRef\]](#)
35. Ghampson, I.T.; Canales, R.; Escalona, N. A study of the hydrodeoxygenation of anisole over Re-MoOx/TiO₂ catalyst. *Appl. Catal. A Gen.* **2018**, *549*, 225–236. [\[CrossRef\]](#)
36. Bjelić, A.; Grilc, M.; Likozar, B. Catalytic hydrogenation and hydrodeoxygenation of lignin-derived model compound eugenol over Ru/C: Intrinsic microkinetics and transport phenomena. *Chem. Eng. J.* **2018**, *333*, 240–259. [\[CrossRef\]](#)
37. Zhu, C.; Cao, J.P.; Zhao, X.Y.; Xie, T.; Zhao, M.; Wei, X.Y. Bimetallic effects in the catalytic hydrogenolysis of lignin and its model compounds on Nickel-Ruthenium catalysts. *Fuel Process. Technol.* **2019**, *194*, 106126. [\[CrossRef\]](#)
38. Lu, M.; Du, H.; Wei, B.; Zhu, J.; Li, M.; Shan, Y.; Shen, J.; Song, C. Hydrodeoxygenation of Guaiacol on Ru Catalysts: Influence of TiO₂-ZrO₂ Composite Oxide Supports. *Ind. Eng. Chem. Res.* **2017**, *56*, 12070–12079. [\[CrossRef\]](#)
39. Pan, C.J.; Tsai, M.C.; Su, W.N.; Rick, J.; Akalework, N.G.; Agegnehu, A.K.; Cheng, S.-Y.; Hwang, B.-J. Tuning/exploiting Strong Metal-Support Interaction (SMSI) in Heterogeneous Catalysis. *J. Taiwan Inst. Chem. Eng.* **2017**, *74*, 154–186. [\[CrossRef\]](#)

40. Massoth, F.E.; Politzer, P.; Concha, M.C.; Murray, J.S.; Jakowski, J.; Simons, J. Catalytic hydrodeoxygenation of methyl-substituted phenols: Correlations of kinetic parameters with molecular properties. *J. Phys. Chem. B* **2006**, *110*, 14283–14291. [[CrossRef](#)]
41. Mortensen, P.M.; Grunwaldt, J.D.; Jensen, P.A.; Jensen, A.D. Screening of catalysts for hydrodeoxygenation of phenol as a model compound for bio-oil. *ACS Catal.* **2013**, *3*, 1774–1785. [[CrossRef](#)]
42. Broglia, F.; Rimoldi, L.; Meroni, D.; de Vecchi, S.; Morbidelli, M.; Ardizzone, S. Guaiacol hydrodeoxygenation as a model for lignin upgrading. Role of the support surface features on Ni-based alumina-silica catalysts. *Fuel* **2019**, *243*, 501–508. [[CrossRef](#)]
43. Sirous-Rezaei, P.; Jae, J.; Cho, K.; Ko, C.H.; Jung, S.C.; Park, Y.K. Insight into the effect of metal and support for mild hydrodeoxygenation of lignin-derived phenolics to BTX aromatics. *Chem. Eng. J.* **2019**, *377*, 120121. [[CrossRef](#)]
44. Gonçalves, V.O.O.; Brunet, S.; Richard, F. Hydrodeoxygenation of Cresols Over Mo/Al₂O₃ and CoMo/Al₂O₃ Sulfided Catalysts. *Catal. Lett.* **2016**, *146*, 1562–1573. [[CrossRef](#)]
45. Venkatesan, K.; Krishna, J.V.J.; Anjana, S.; Selvam, P.; Vinu, R. Hydrodeoxygenation kinetics of syringol, guaiacol and phenol over H-ZSM-5. *Catal. Commun.* **2021**, *148*, 106164. [[CrossRef](#)]
46. Prasomsri, T.; To, A.T.; Crossley, S.; Alvarez, W.E.; Resasco, D.E. Catalytic conversion of anisole over HY and HZSM-5 zeolites in the presence of different hydrocarbon mixtures. *Appl. Catal. B* **2011**, *106*, 204–211. [[CrossRef](#)]
47. Ji, J.; Duan, X.; Qian, G.; Zhou, X.; Tong, G.; Yuan, W. Towards an efficient CoMo/ γ -Al₂O₃ catalyst using metal amine metallate as an active phase precursor: Enhanced hydrogen production by ammonia decomposition. *Int. J. Hydrogen Energy* **2014**, *39*, 12490–12498. [[CrossRef](#)]
48. Tavizón-Pozos, J.A.; Santolalla-Vargas, C.E.; Valdés-Martínez, O.U.; de los Reyes Heredia, J.A. Effect of metal loading in unpromoted and promoted CoMo/Al₂O₃-TiO₂ catalysts for the hydrodeoxygenation of phenol. *Catalysis* **2019**, *9*, 550. [[CrossRef](#)]
49. Reddy, B.M.; Khan, A. Recent advances on TiO₂-ZrO₂ mixed oxides as catalysts and catalysts supports. *Catal. Rev. Sci. Eng.* **2005**, *47*, 257–296. [[CrossRef](#)]
50. Maity, S.K.; Ancheyta, J.; Soberanis, L.; Alonso, F.; Llanos, M.E. Alumina-titania binary mixed oxide used as support of catalysts for hydrotreating of Maya heavy crude. *Appl. Catal. A Gen.* **2003**, *244*, 141–153. [[CrossRef](#)]
51. Maity, S.; Rana, M.; Bej, S.; Ancheyta-Juárez, J.; Murali Dhar, G.; Prasada Rao, T. TiO₂-ZrO₂ mixed oxide as a support for hydrotreating catalyst. *Catal. Lett.* **2001**, *72*, 115–119. [[CrossRef](#)]
52. Vo, T.K.; Kim, W.S.; Kim, S.S.; Yoo, K.S.; Kim, J. Facile synthesis of Mo/Al₂O₃-TiO₂ catalysts using spray pyrolysis and their catalytic activity for hydrodeoxygenation. *Energy Convers. Manag.* **2018**, *158*, 92–102. [[CrossRef](#)]
53. Vakros, J.; Lycourghiotis, A.; Voyiatzis, G.A.; Siokou, A.; Kordulis, C. CoMo/Al₂O₃-SiO₂ catalysts prepared by co-equilibrium deposition filtration: Characterization and catalytic behavior for the hydrodesulfurization of thiophene. *Appl. Catal. B* **2010**, *96*, 496–507. [[CrossRef](#)]
54. Tavizón-Pozos, J.A.; Suárez-Toriello, V.A.; de Los Reyes Heredia, J.A.; Guevara-Lara, A.; Pawelec, B.; Fierro, J.L.G.; Vrinat, M.; Geantet, C. Deep Hydrodesulfurization of Dibenzothiophenes over NiW Sulfide Catalysts Supported on Sol-Gel Titania-Alumina. *Top. Catal.* **2016**, *59*, 241–251. [[CrossRef](#)]
55. Murali Dhar, G.; Srinivas, B.N.; Rana, M.S.; Kumar, M.; Maity, S.K. Mixed oxide supported hydrodesulfurization catalysts—A review. *Catal. Today* **2003**, *86*, 45–60. [[CrossRef](#)]
56. Pinzón-Ramos, I. Kinetic Evaluation of CoMo Materials Supported on Alumina/Titania in Phenol Hydrodeoxygenation Reactions. Master's Thesis, Metropolitan Autonomous University, Ciudad de Mexico, Mexico, 2019. [[CrossRef](#)]
57. Shetty, M.; Anderson, E.M.; Green, W.H.; Román-Leshkov, Y. Kinetic analysis and reaction mechanism for anisole conversion over zirconia-supported molybdenum oxide. *J. Catal.* **2019**, *376*, 248–257. [[CrossRef](#)]
58. Tan, Q.; Wang, G.; Long, A.; Dinse, A.; Buda, C.; Shabaker, J.; Resasco, D.E. Mechanistic analysis of the role of metal oxophilicity in the hydrodeoxygenation of anisole. *J. Catal.* **2017**, *347*, 102–115. [[CrossRef](#)]
59. Thommes, M.; Kaneko, K.; Neimark, A.; Olivier, J.P.; Rodriguez-Reinoso, F.; Rouquerol, J.; Sing, K.S.W. physisorption of gases, with special reference to the evaluation of surface area and pore size distribution (IUPAC Technical Report). *Pure Appl. Chem.* **2015**, *87*, 1051–1069. [[CrossRef](#)]
60. Platanitis, P.; Panagiotou, G.D.; Bourikas, K.; Kordulis, C.; Fierro, J.L.G.; Lycourghiotis, A. Preparation of un-promoted molybdenum HDS catalysts supported on titania by equilibrium deposition filtration: Optimization of the preparative parameters and investigation of the promoting action of titania. *J. Mol. Catal. A Chem.* **2016**, *412*, 1–12. [[CrossRef](#)]
61. Gajardo, P.; Grange, P.; Delmon, B. Structure of Oxide CoMo/ γ -Al₂O₃ Hydrodesulfurization Catalysts: An XPS and DRS Study. *J. Catal.* **1980**, *63*, 201–216. [[CrossRef](#)]
62. Water, L.G.A.; Bezemer, G.L.; Bergwerff, J.A.; Versluijs-Helder, M.; Weckhuysen, B.M.; de Jong, K.P. Spatially resolved UV-vis microspectroscopy on the preparation of alumina-supported Co Fischer-Tropsch catalysts: Linking activity to Co distribution and speciation. *J. Catal.* **2006**, *242*, 287–298. [[CrossRef](#)]
63. Vrinat, M.; Letourneur, D.; Bacaud, R.; Harlé, V.; Jouguet, B.; Leclercq, C. CoMo/Al₂O₃ and CoMo/TiO₂-Al₂O₃ catalysts in hydrodesulfurization: Relationship between the promoting effect of cobalt and the nature of the support. *Elsevier Sci.* **1999**, *127*, 153–160. [[CrossRef](#)]
64. Yocupicio, R.I.; Díaz De León, J.N.; Zepeda, T.A.; Fuentes, S. Estudio de catalizador CoMo soportado en zeolitas mesoporosas jerárquicas para hidrodesulfuración de dibenzotiofeno. *Rev. Mex. Ing. Quim.* **2017**, *16*, 503–520.

65. Papadopoulou, C.; Vakros, J.; Matralis, H.K.; Kordulis, C.; Lycourghiotis, A. On the relationship between the preparation method and the physicochemical and catalytic properties of the CoMo/ γ -Al₂O₃ hydrodesulfurization catalysts. *J. Colloid Interface Sci.* **2003**, *261*, 146–153. [[CrossRef](#)]
66. Alvarez-Amparán, M.A.; Rodríguez-Gomeztagle, J.; Cedeño-Caero, L. Efecto del método de preparación de catalizadores de MoO₃/Al₂O₃ para la desulfuración oxidativa de un diesel modelo. *Rev. Mex. Ing. Quim.* **2015**, *28*, 40–47.
67. Williams, C.C.; Ekerdt, J.G.; Jehng, J.-M.; Hardcastle, F.D.; Wachs, I.E. A Raman and Ultraviolet Diffuse Reflectance Spectroscopic Investigation of Alumina-Supported Molybdenum Oxide. *J. Phys. Chem.* **1991**, *95*, 8781–8791. [[CrossRef](#)]
68. Bergwerff, J.A.; Visser, T.; Weckhuysen, B.M. On the interaction between Co- and Mo-complexes in impregnation solutions used for the preparation of Al₂O₃-supported HDS catalysts: A combined Raman/UV-vis-NIR spectroscopy study. *Catal. Today* **2008**, *130*, 117–125. [[CrossRef](#)]
69. Jeziorowski, H.; Knozinger, H. Raman and Ultraviolet Spectroscopic Characterization of Molybdena on Alumina Catalysts. *J. Phys. Chem.* **1979**, *83*, 1166–1173. [[CrossRef](#)]
70. Thielemann, J.P.; Ressler, T.; Walter, A.; Tzolova-Müller, G.; Hess, C. Structure of molybdenum oxide supported on silica SBA-15 studied by Raman, UV-vis and X-ray absorption spectroscopy. *Appl. Catal. A Gen.* **2011**, *399*, 28–34. [[CrossRef](#)]
71. Zhu, Y.; Zhang, Y.; Dan, Y.; Yuan, Y.; Zhang, L.; Li, W.; Li, D. optimization of reaction variables and macrokinetics for the hydrodeoxygenation of full range low temperature coal tar. *React. Kinet. Mech. Catal.* **2015**, *116*, 433–450. [[CrossRef](#)]
72. Box, G.E.P.; Draper, N.R. *Response Surfaces, Mixtures, and Ridge Analyses*, 2nd ed.; Wiley: Madison, WI, USA, 2007; Chapter 15; Volume 1, pp. 495–498, ISBN 978-0-470-05357-7.